

Article

Improving Line Current Distortion in Single-Phase Vienna Rectifiers Using Model-Based Predictive Control

Yong-Dae Kwon, Jin-Hyuk Park and Kyo-Beum Lee * 

Department of Electrical and Computer Engineering, Ajou University, 206, World cup-ro, Yeongtong-gu, Suwon 16499, Korea; kwon911222@gmail.com (Y.-D.K.); powerword87@gmail.com (J.-H.P.)

* Correspondence: kyl@ajou.ac.kr; Tel.: +82-31-219-2487

Received: 21 April 2018; Accepted: 10 May 2018; Published: 12 May 2018



Abstract: Conventional single-phase Vienna rectifiers employ proportional-integral (PI) controllers which are appropriate for controlling DC components, to regulate their line currents. However, in the regions close to the line current's zero-crossing point, the dynamics of PI controllers are too slow to respond to the reference current, which has an AC component. Hence, the power factor (PF) of the device is degenerated, and total harmonic distortion (THD) increases. A controller with a fast dynamic response is thus required to solve this problem. In this paper, we investigate the use of a model-based predictive controller (MPC), which has a faster dynamic response than a PI controller, to improve the line current quality of a single-phase Vienna rectifier. With this method, the average current in both the continuous current mode (CCM) and the discontinuous current mode (DCM) of operation are controlled using a mode detection method. Moreover, we calculate the optimized duty cycle for the single-phase Vienna rectifier, by predicting the next current state. We verify the operation of the proposed algorithm using a PSIM simulation, and a practical experiment conducted with a 1-kW-rated single-phase Vienna rectifier prototype. With the proposed method, the quality of the line current near the zero-crossing point is improved, and the PF is controlled to unity.

Keywords: predictive control; E.V. charger; controllable rectifier; single-phase Vienna rectifier; power factor correction; on board charger

1. Introduction

Recently, there has been a growing interest in eco-friendly electric vehicle (EV) systems, because of the depletion of fossil-fuels, and in order to reduce greenhouse gas emissions [1]. With the development of EV systems, the demand for related infrastructure has also increased. In particular, the development of chargers for EV systems remains the biggest infrastructure-related issue. An EV charger consists of two parts [2–4], one to deliver energy from the AC grid to the DC link, and another to deliver energy from the DC link to the battery [5–7]. Two different circuits can be considered for construction of the AC to DC conversion system: a bidirectional inverter, which is capable of AC-DC and DC-AC conversion, and a unidirectional Vienna rectifier, which is only capable of AC-DC conversion. As a fast charging characteristic and high efficiency are required of EV chargers, the Vienna rectifier, which has a simple structure and high efficiency, is typically used as the pulse-width modulation (PWM) converter in this device, to control the grid side current [8–11].

The Vienna rectifier discussed in this paper is similar in structure to a T-type inverter. However, in this device the outer switches are substituted for diodes, D_p and D_n , as shown in Figure 1, which restrict the flow of energy from DC to AC. Furthermore, we consider a single-phase topology, for application to the on board charger (OBC) of an EV, because of the simplified structure of this configuration, and its use of fewer switching devices [12–15].

To control a Vienna rectifier in normal operation, the “important rule”, defined as the sign of the voltage being equal to the sign of the current, should be satisfied. Failure to meet this criterion contributes to the degradation of current quality and an increase in total harmonic distortion (THD) [16]. Conventional Vienna rectifiers apply proportional-integral (PI) controllers to the line current control loop. These devices are optimized for regulating DC, and not AC components [17], as their dynamic response is not fast enough to control alternating current. Hence, an appropriate output cannot be estimated if a PI controller is used in an AC current control loop [18], and THD of the line current consequently increases [19,20]. Therefore, as the line current frequency increases and the system power decreases, the line current distortion problem becomes dominant [21].

In addition to large errors and the slow dynamic response of the PI controller, another reason for current distortion is a difference between the sensed current and the average current caused by discontinuous current mode (DCM) operation around the input voltage’s zero crossing point [22]. The phase difference between the input voltage and the line current also increases around this neutral region. Thus, to reduce the response error and alleviate problems associated with the DCM, a controller that has a fast dynamic response and can control the power factor (PF) to unity is necessary [23–28].

The predictive control method was researched to make the controller with faster dynamics. The predictive control is designed with the system model. Generally, in this method, the current is predicted by the past state data. The optimal duty cycle is derived by using this predicted current. Hence, the controller is possible to get the faster dynamics than the PI control method. As mentioned before, in order to deduce the optimal duty cycle, the current prediction is one of the important procedure. The study of [29] was considered for the next current prediction. The inductance model and simple mathematical method is used for calculating the predicted current.

In this paper, we propose a model-based predictive control algorithm for a single-phase Vienna rectifier, to improve the quality of its line current. The proposed controller has fast dynamics and simple algorithm. The optimal duty cycle for regulating the reference current in the shortest timescale is deduced by the controller algorithm predicting the next current state, and subsequently minimizing the error between the reference current and the line current. In addition, to control the rectifier in continuous current mode (CCM) and DCM operation separately, a mode detection algorithm is adopted. Hence, different optimized duty cycles for controlling the line current in CCM and DCM are deduced. In spite of this, the algorithm is capable of controlling the average line current, even if these two modes of operation are mixed. In contrast to PI control, the proposed algorithm has a fast dynamic response, making it possible for the line current to follow the reference current with the smallest error. Hence, the PF can be controlled to unity and THD of the line current can be decreased. We verify the operation of the proposed control algorithm using PSIM simulation and practical experiments performed with a 1-kW-rated single-phase Vienna rectifier prototype. Moreover, we compare the line current of a rectifier controlled using a conventional PI algorithm and the proposed algorithm, to demonstrate its performance.

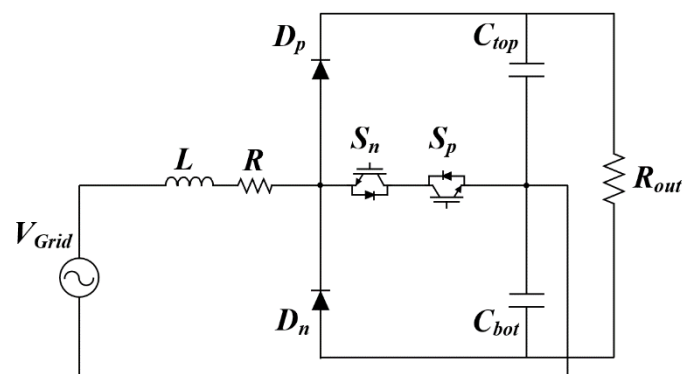


Figure 1. Circuit diagram of a single-phase Vienna rectifier system.

2. Vienna Rectifier Control

2.1. Operation of the Vienna Rectifier

A circuit diagram of the single-phase Vienna rectifier employed in this study is shown in Figure 1. To the grid side, input filter of this topology is composed of inductor, L . The resistor, R , means the resistive component in the inductor. As previously stated, the topology of this device is similar to that of a single-phase T-type inverter, with the outer switches of the inverter having been replaced by the diodes D_p and D_n in the rectifier. The rectifier topology includes two inner switches, a top switch, S_p , which only operates when the top capacitor, C_{top} , is charging, and a bottom switch, S_n , which only operates while the bottom capacitor, C_{bot} , is charging. The detail nomenclature of the components is shown in Table A1 in appendix A. Figure 2 shows the equivalent circuit and the current path of a single-phase Vienna rectifier when the top switch is in operation. Figure 3 shows the equivalent circuit and the current path of a single-phase Vienna rectifier when the bottom switch is in operation.

Figures 2 and 3 are further subdivided into different modes. Mode 1 and Mode 2 are operational when the grid voltage is positive, and Mode 3 and Mode 4 operate when the grid voltage is negative. When Mode 1 is in operation, both switches, S_p and S_n , are turned off. The line current flows through the top diode, D_p , and charges C_{top} . In Mode 2, S_p is turned on and the line current flows through this switch and the anti-parallel diode of S_n . The closed current path consists of the switching device and the neutral point of the DC link to the grid. The current path in Mode 3 is as with Mode 2. However, the direction of current flow is reversed in this mode. In Mode 4, S_n is turned off and current flow from the DC link to the grid side is in the same direction as in Mode 3. In this mode, the current path includes the bottom diode.

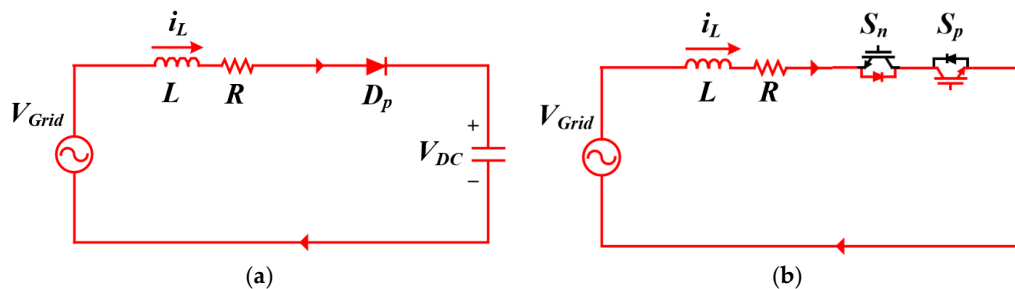


Figure 2. Equivalent circuit of a rectifier when the top switch is in operation. (a) Mode 1; (b) Mode 2.

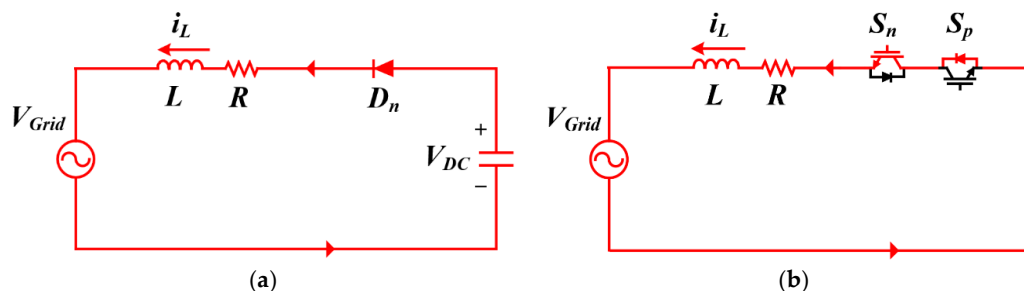


Figure 3. Equivalent circuit of a rectifier when the bottom switch is in operation. (a) Mode 3; (b) Mode 4.

2.2. Conventional PI Control of a Vienna Rectifier

A block diagram of a complete Vienna rectifier system, including control circuitry, is shown in Figure 4. The voltage controller comprising the outer control loop consists of a PI controller, the input to which is the error between the sensed DC link voltage and the reference DC link voltage. The voltage controller of the conventional and proposed method applied system is same, both are PI controller. The output of the voltage controller is the reference current. In this image, $\sin\omega t$ is the waveform of the

grid voltage, which is obtained by dividing the sensed grid voltage by its magnitude. The final line current reference, i_L^* , is obtained by multiplying i^* with $\sin\omega t$. The input to the inner current control loop is the error between the sensed line current, i_L , and i_L^* . A PI controller is adopted for the current controller, the output of which is the PWM duty cycle. The bandwidth, ω_{cc} , of the current control loop should be wider than that of the voltage control loop. In addition, to prevent noise and disturbance, this ω_{cc} should be 1/20 or 1/10 of the switching frequency. Hence, the ω_{cc} of the system is limited by the switching frequency.

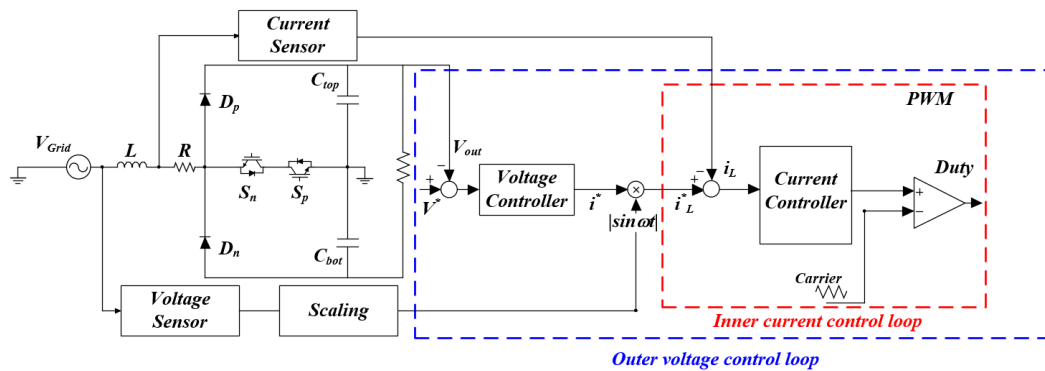


Figure 4. Block diagram of a single-phase Vienna rectifier system.

Figure 5 shows the closed current loop of the PI controller applied system. The $G_{PI}(s)$ means the model of PI controller and $G_{plant}(s)$ means the large signal mode of plant. $G_{PI}(s)$ and $G_{plant}(s)$ can be expressed as:

$$G_{PI}(s) = K_{p,current}(s) + \frac{K_{I,current}}{s}, \quad G_{plant}(s) = \frac{1}{sL}, \quad (1)$$

where $K_{p,current}$ is proportional gain (or P gain) of the current controller, $K_{I,current}$ is integral gain (or I gain) of the current controller, L is the inductance of system. From (1) the closed current loop transfer function based on PI controller equation can be expressed as:

$$T(s) = \frac{G_{PI}G_{plant}}{1 + G_{PI}G_{plant}}, \quad (2)$$

Hence, the closed current loop transfer function based on PI controller, $T(s)$, can be derived as:

$$T(s) = \frac{\frac{K_{I,current}}{Ls^2} + \frac{K_{p,current}}{Ls}}{\frac{K_{I,current}}{Ls^2} + \frac{K_{p,current}}{Ls} + 1}. \quad (3)$$

By the characteristic equation of this transfer function, the P and I gain are simply derived as:

$$K_{p,current} = 2\zeta\omega_{cc}L, \quad K_{I,current} = \omega_{cc}^2L. \quad (4)$$

where ζ is the damping-ratio. This value usually set as 0.707 for the critical damping characteristic. In (4) the gain of the PI controller contains the ω_{cc} . Thus, the gain of the controller is also limited by the switching frequency. As the gain of the PI controller employed in the current controller is limited, the regulation of the current is diminished when the input voltage crosses zero. As a result of the minimal control at this point, the current becomes distorted. One reason for this distortion is the slow dynamic response of the PI controller. The bandwidth of the controller is limited by the switching frequency, which also affects the dynamic response. The change in the AC reference around the zero-crossing section occurs too quickly for the controller to respond. The second reason for distortion is the variable mode of operation of the rectifier. In the CCM region, the average inductor current is

equal to the sensed current. This means that the average current follows the reference current. In the DCM region, the average current does not match the sensed current and it thus cannot follow the reference current. Hence, a controller with a fast dynamic response and a mode detection algorithm is required to solve these problems.

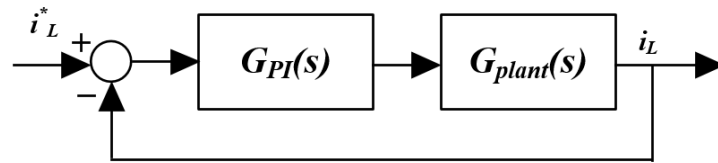


Figure 5. Closed current loop of the PI controller applied system.

2.3. Model-Based Predictive Control of a Single-Phase Vienna Rectifier

The model-based predictive control algorithm predicts the next current state and calculates the optimal duty cycle using data from previous states. Unlike the conventional PI control algorithm, this technique has a fast dynamic response, suitable for control of AC components. Therefore, it is possible to improve the line current distortion of the single-phase Vienna rectifier using the proposed algorithm. However, in the real situation when using a digital signal process (DSP), there is one cycle delay for an analog to digital conversion (ADC). Hence, in order to solve this problem, current prediction of two cycle after state is applied. Moreover, the precision of the model affects the performance of the controller. Thus, the compensation method for precise inductance model should be considered for the modelling of the controller.

2.3.1. Estimating the Gradient of the Inductor Current

The optimal duty cycle of a Vienna rectifier is derived using the predicted current and the gradient of the current flowing through the inductor. However, mode detection is required, as the shape of the line current is different in DCM and CCM operation. Hence, a mode detection method is also considered in addition to the current control method proposed in this paper.

The current paths, when the top switch is off or on, are shown in Figure 6a,b, respectively. When the input voltage, V_{Grid} , is positive, the current flows through the switches if S_p is on, and through D_p if S_p is off. The voltage equation when the switch is on can be expressed as:

$$|V_{Grid}| - V_L = |V_{Grid}| - \left(L \frac{di_L}{dt} + i_L R \right) = 0, \quad (5)$$

where V_L is the voltage across the inductor and i_L is the inductor current that passes the resistor. The voltage applied to the inductor can be divided into two parts, one is voltage across the inductance component and another is voltage across the resistance of inductor. Equation (5) can be rearranged to obtain an expression for the slope, di_L/dt . Based on this rearranged equation, the slope of the current through the inductor when the switch is on, $S_{L,on}$, can be expressed as:

$$S_{L,on} = \frac{di_L}{dt} = \frac{|V_{Grid}| - i_L R}{L}. \quad (6)$$

As V_{Grid} is positive in this sector, $S_{L,on}$ is also positive. The voltage equation when the switch is off can be expressed as:

$$|V_{Grid}| = V_{top} + V_L = V_{top} + L \frac{di_L}{dt} + i_L R, \quad (7)$$

where V_{top} is the voltage of the top DC link. As performed previously, (5) can be rearranged for the slope of the current as:

$$S_{L,top,off} = \frac{di_L}{dt} = \frac{|V_{Grid}| - i_L R - V_{top}}{L}, \quad (8)$$

where $S_{L,top,off}$ is the slope of the inductor current when the top switch is off. As the DC link voltage is larger than $|V_{Grid}|$ in the steady state, the value of the slope is negative. In this equation the DC link voltage is the difference between V_{top} and V_{bot} . Hence, the expression calculated for $S_{L,top,off}$ is only suitable for when the top switch is in operation, and a different equation is required for the slope of the inductor current when the bottom switch is off. This can be obtained by substituting V_{bot} for V_{top} .

The slope of the inductor current when the bottom switch is in operation can be expressed similarly to (5)–(8). The equation for the current slope when the bottom switch is on is the same as (5), as the input voltage is an absolute value. However, when the bottom switch is off, V_{bot} is applied. Hence, the DC link voltage of the bottom capacitor, V_{bot} , is used instead of V_{top} , in the slope equation. The slope of the inductor current when the bottom switch is off, $S_{L,bot,off}$, can be expressed as:

$$S_{L,bot,off} = \frac{di_L}{dt} = \frac{|V_{Grid}| - i_L R - V_{bot}}{L} \tag{9}$$

The optimal duty cycle can thus be calculated using the slope equations given in (6), (8) and (9). However, considering the “skin effect” in the inductor, the R in slope equation has small value which is enough to ignore.

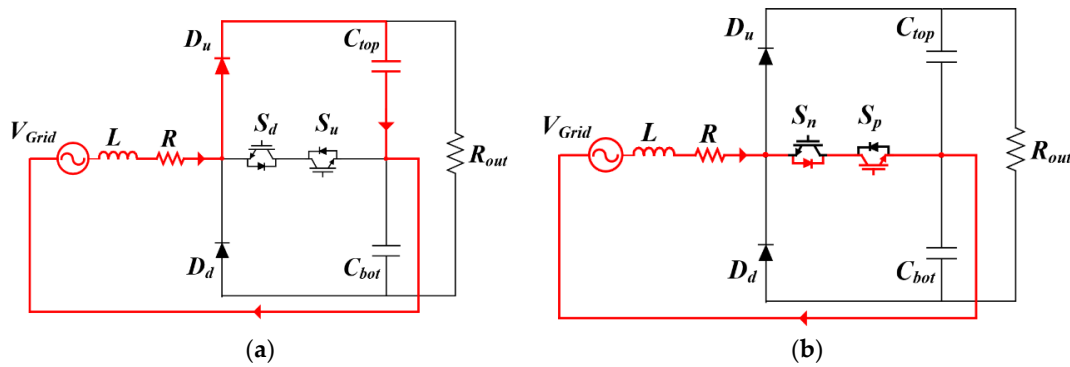


Figure 6. Current path of the single-phase Vienna rectifier. (a) Operation when the top switch is off; (b) Operation when the top switch is on.

2.3.2. Deriving the Optimal Duty Cycle for CCM Operation

The inductor current during CCM, and the gate signal in the steady state region, are shown in Figure 7. In the steady state CCM region, the inductor current sensed by the digital processor is equal to the average inductor current. As such, the next inductor current state, $i_{L,k+1}$, can be calculated using the current slopes previously derived as (6)–(8), and the present inductor current state, $i_{L,k}$, as:

$$i_{L,k+1,top} = i_{L,k} + S_{L,on}T_{on,top} + S_{L,top,off} \cdot (T_s - T_{on,top}), \tag{10}$$

where $T_{on,top,CCM}$ is the period the top switch is on during CCM, T_{off} in Figure 7 is the period the switch is off, and T_s is the sampling period, which is the sum of T_{on} and T_{off} . The error, i_{err} , between $i_{L,k+1}$ and the line current reference, i_L^* , can be expressed as follows:

$$i_{err,top} = i_L^* - i_{L,k+1,top} = i_L^* - i_{L,k} - S_{L,on}T_{on,top} - S_{L,top,off} \cdot (T_s - T_{on,top}) = 0. \tag{11}$$

By rearranging (11), the on time interval for the duty cycle of the top switch can be derived as follows:

$$T_{on,top,CCM} = \frac{i_L^* - i_{L,k} - S_{L,top,off} \cdot T_s}{S_{L,on} - S_{L,top,off}}. \tag{12}$$

The optimal duty cycle for the top switch during CCM, $Duty_{top,CCM}$, can be expressed as follows:

$$Duty_{top,CCM} = \frac{T_{on,top,CCM}}{T_s} \tag{13}$$

The optimal duty cycle of the bottom switch during CCM, $Duty_{bot,CCM}$, can be derived in a similar manner. Using the inductor current slope of the bottom switch, $Duty_{bot,CCM}$ can be written as:

$$T_{on,bot,CCM} = \frac{i_L^* - i_{L,k} - S_{L,bot,off} \cdot T_s}{S_{L,on} - S_{L,bot,off}}, \tag{14}$$

$$Duty_{bot,CCM} = \frac{T_{on,bot,CCM}}{T_s}, \tag{15}$$

where $T_{on,bot,CCM}$ is the period of time that the bottom switch is on during CCM.

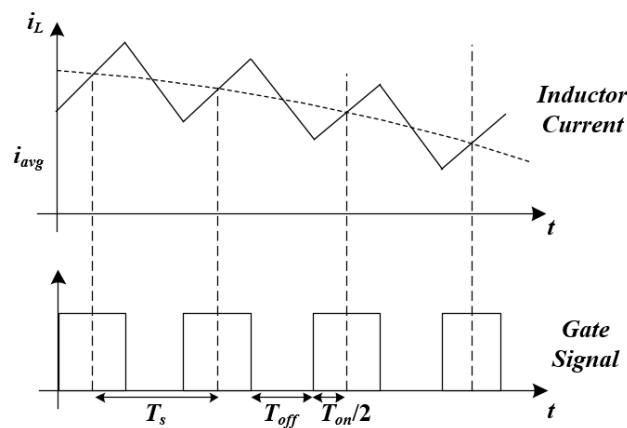


Figure 7. Control signals for a model-based predictive controller (MPC) in CCM.

2.3.3. Deriving the Optimal Duty Cycle for DCM Operation

The steady state inductor current and gate signal during DCM are shown in Figure 8. In this mode of operation, the average inductor current is different to the sensed inductor current. Furthermore, the sum of the rise time and fall time does not correspond to the value of T_s . Hence, the inductor current is improperly regulated with respect to the applied reference current when the current control algorithm developed for CCM is applied in DCM. An appropriate optimal duty cycle prediction method is thus required for DCM.

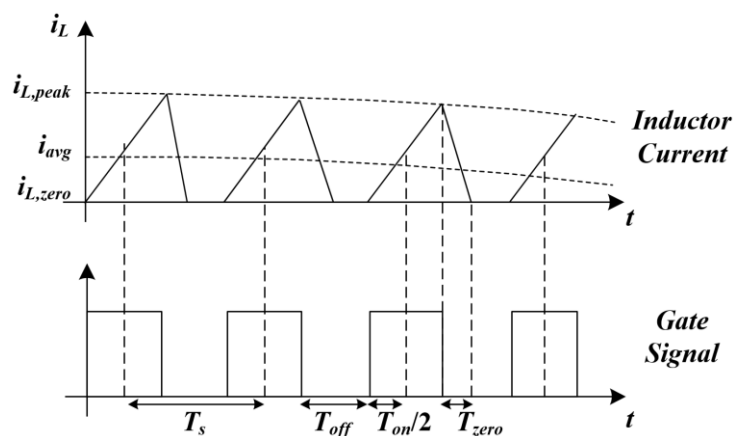


Figure 8. Control signals for a MPC in DCM.

The optimal duty cycle for DCM operation can be deduced by applying a similar method to that used for CCM. The peak inductor current equation can be expressed as follows:

$$i_{L,peak} = S_{L,on} \cdot T_{on} = -S_{L,top,off} \cdot T_{zero}, \quad (16)$$

where T_{zero} is the time required for $i_{L,peak}$ to be reduced to $i_{L,zero}$. From (16), T_{zero} can be expressed as:

$$T_{zero} = -\frac{S_{L,on} T_{on}}{S_{L,top,off}}. \quad (17)$$

In DCM, the next average inductor current state can be calculated using integration as follows:

$$i_{L,avg,k+1} = \frac{1}{T_s} \int_{T_s} i_L dt = \frac{i_{L,peak} \cdot (T_{on} + T_{zero})}{2 \cdot T_s}. \quad (18)$$

The error can be calculated in a similar manner to (10) as:

$$i_{err,DCM} = i_L^* - i_{L,avg,k+1}. \quad (19)$$

By rearranging (19), the on time interval can be expressed as follows:

$$T_{on,top,DCM} = \sqrt{2 \cdot i_L^* \cdot T_s / S_{L,on} \cdot \left(1 - \frac{S_{L,on}}{S_{L,top,off}}\right)}, \quad (20)$$

where $T_{on,top,DCM}$ is the duration the top switch is on during DCM. The optimal duty cycle of the top switch during DCM, $Duty_{top,DCM}$, can be expressed as follows:

$$Duty_{top,DCM} = \frac{T_{on,top,DCM}}{T_s}. \quad (21)$$

The optimal duty cycle of the bottom switch during DCM, $Duty_{bot,DCM}$, can be derived in a similar manner. Using the current slope expression for the bottom switch, $Duty_{bot,DCM}$ can be written as:

$$T_{on,bot,DCM} = \sqrt{2 \cdot i_L^* \cdot T_s / S_{L,on} \cdot \left(1 - \frac{S_{L,on}}{S_{L,bot,off}}\right)}, \quad (22)$$

$$Duty_{bot,DCM} = \frac{T_{on,bot,DCM}}{T_s}, \quad (23)$$

where $T_{on,bot,DCM}$ is the period the bottom switch is on during DCM. Using the optimal duty cycles calculated with (13), (15), (21) and (23), it is possible to control the system with a faster dynamic response than a PI controller.

2.3.4. Mode Detection for the Vienna Rectifier

The average current in both the heavy load and light load conditions are controllable using the duty cycles optimized for CCM and DCM operation, respectively. However, in the medium load condition where both conduction modes coexist, the appropriate control method should be determined for the relevant mode of operation. During DCM operation, the duty cycle calculated using the CCM equation is always larger than the duty cycle calculated using the DCM equation. In contrast, during CCM operation, the duty cycle calculated using the DCM equation is always larger than the duty cycle calculated using the CCM equation. Therefore, by verifying the smaller duty cycle in the present state of operation, it is possible to select the appropriate duty cycle for each mode. Figure 9 shows the operation of the mode detection method. The regions where the duty cycles for CCM and DCM

intersect are shown in Figure 9a. At these intersection points, the conduction mode of the rectifier changes. By applying the criterion defined in the mode detection method, it is possible to select the optimal duty cycle for the relevant conduction mode, as illustrated in Figure 9b.

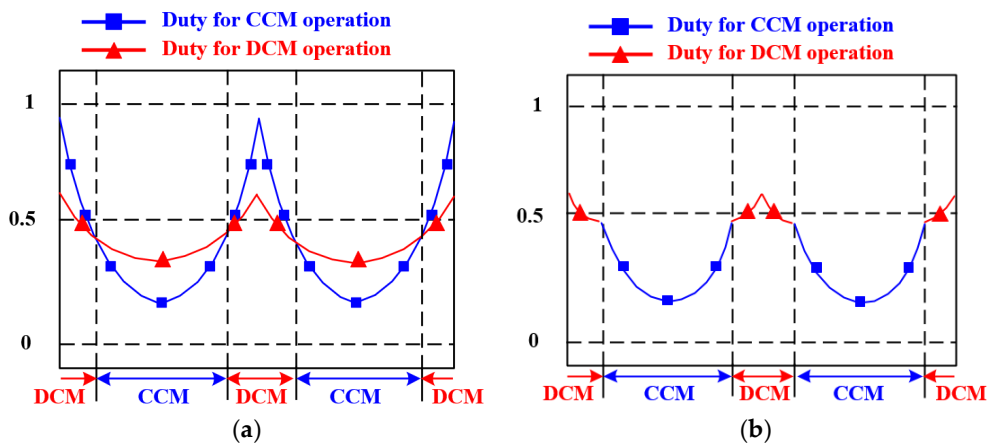


Figure 9. Operation of mode detection algorithm. (a) Intersection of CCM and DCM duty cycles; (b) Optimal duty cycle for mixed mode operation.

2.3.5. System Stability of Proposed Predictive Control Method

The proposed method calculates the optimal duty cycle by the inductance value. Hence, the performance of controller depends on the preciseness of the inductance model. The inductance value can be changing by the experimental ambient. Therefore, it is important to consider this inductance value variation. In order to confirm the stability of the proposed method, z-plane discriminant analysis is used. The block diagram of simple system model is shown in Figure 10.

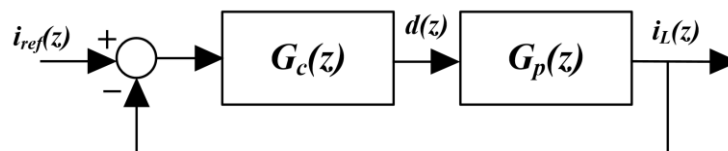


Figure 10. Block diagram of simple system model.

The rectifier system is simply derived by the small signal model of the voltage equation of inductor as:

$$G_p(s) = \frac{i_L(s)}{d(s)} = \frac{V_{DC}}{sL_0}, \tag{24}$$

where, L_0 is the actual inductance value with considering inductance value changing. Then changing this equation to the z-domain the equation is rearranged as:

$$G_p(z) = \frac{i_L(z)}{d(z)} = \frac{V_{DC}T_s}{L_0} \left(\frac{z^{-1}}{1 - z^{-1}} \right), \tag{25}$$

As shown in this figure, z-domain equation of the controller is simply model with the (5), (7) and (11) as:

$$G_c(z) = \frac{d(z)}{i_e(z)} = \frac{L_{cal}}{V_{DC}T_s}, \tag{26}$$

where L_{cal} is the nominal inductance value without considering of inductance value changing. The transfer function of the system is derived by (25) and (26) as:

$$H(z) = \frac{G_c(z)G_p(z)}{1 + G_c(z)G_p(z)} = \frac{z^{-1}}{1 + (K - 1)z^{-1}}, \quad (27)$$

where $K = (L_{cal}/L_0)$. From (27), the system pole is calculated as:

$$z = 1 - K. \quad (28)$$

The system pole is in the unit circle on the z-plane, it is possible to confirm the system is stable. Figure 11 shows the simulation results of system poles of the proposed controller on z-plane with using MATLAB. When the L_0 is changed to the 50% error of its value, the system pole is on the unit circle and the L_0 is closer to the L_{cal} the system pole became closer to the origin. Thus, considering this simulation results, the inductance error should be less than 50% of L_{cal} in order to make the system stable. As the L_0 increased, the system pole is moving from origin to the positive side of unit circle.

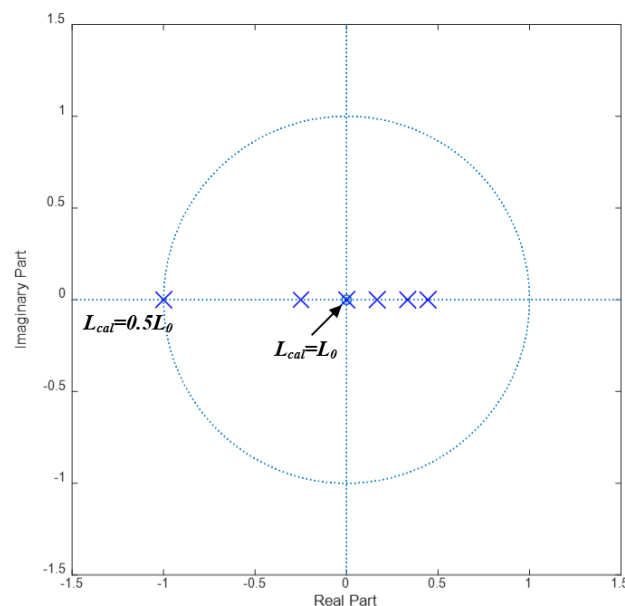


Figure 11. Poles of system on z-plane.

2.3.6. Consideration of Inductance Variation

As mentioned in the previous section, the inductance variation affects to the controllability of the proposed method. The actual inductance value became different to the nominal inductance by the out ambient. This makes the changing of the calculation result of the inductor current slope. Hence, the inductance compensation method is necessary for the proposed control. The researches of [30–32] the compensation method for the inductance is introduced. This paper adopts the simple mathematical method of [32] for the inductance value compensation.

The next inductor current is decided by the next state inductance value and the current state of duty and the inductance value. Hence, by using this relation, the actual inductance is possible to be estimated on line. The equation for the online inductance estimation can be expressed as:

$$L_{k+1} = \left[\frac{i_{L,k} \cdot Duty_k}{i_{L,k+1} \cdot Duty_{k+1}} \right] L_k, \quad (29)$$

where L_k is the current state of online-estimated inductance, L_{k+1} is the current next of online-estimated inductance $i_{L,k}$ is the current state of the inductor current, $i_{L,k+1}$ is the next state of inductor current, $Duty_k$ is the optimal duty cycle in current state and $Duty_{k+1}$.

3. Simulations

To verify the operation of the proposed algorithm, we performed a simulation using PSIM software. Figure 12 shows a schematic of the 1-kW-rated single-phase Vienna rectifier used in simulation. Moreover, both the top and bottom DC voltage are sensed, for calculating the optimal duty cycle of the model-based predictive controller (MPC). The input voltage of the system is $110\text{ V}_{\text{rms}}$, varied at 60 Hz. The DC link voltage is controlled to 350–400 V. The controller should conduct one control operation per one control period because the proposed method should predict the next state current based on system model. Hence the sampling time is selected as $100\ \mu\text{s}$. Detailed simulation parameters are given in Table 1.

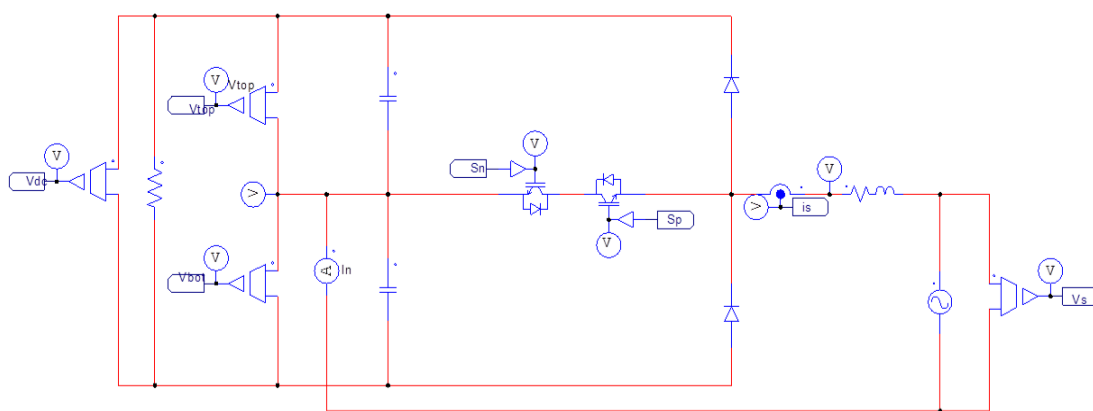


Figure 12. Schematic of the Vienna rectifier used in simulation.

Table 1. Simulation parameters.

Parameter	Value
Rated power	1 kW
Grid side voltage	$110\text{ V}_{\text{rms}}$
DC-link voltage	350–400 V
Inductor	1 mH
Top/Bottom Capacitor	$450\ \mu\text{F}$
Grid frequency	60 Hz
Switching frequency	10 kHz
Sampling time	$100\ \mu\text{s}$

The control algorithms for DCM and CCM operation were verified using a light load condition, defined as 20% of the maximum load, and a heavy load condition, defined as 100% of the maximum load, respectively. To compare the differences between the operation of a PI controller and the MPC, simulations were conducted with a 40% load and a full load. The THD of the resulting current waveforms were used as the standard for comparison.

Figure 13 shows the current waveform derived using the PI controller with a 20% load. The rectifier is in DCM in this load condition, making it difficult for the PI controller to regulate the line current to the reference current. Figure 14 shows the current waveform derived using the PI controller in the 100% load condition. Even though the rectifier is in CCM, the slow dynamic response of the PI controller contributes to the distortion of the line current. Therefore, the line current does not fully mirror the reference current.

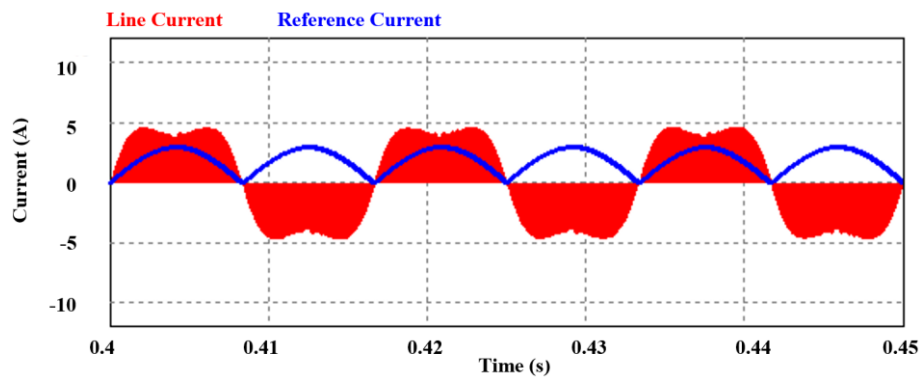


Figure 13. Current waveform derived using PI control in DCM.

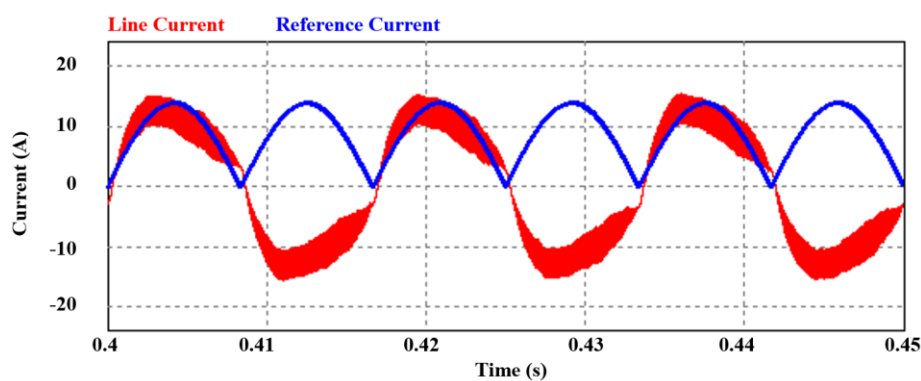


Figure 14. Current waveform derived using PI control in CCM.

Figure 15 shows the current waveform derived using the MPC with a 20% load. Although the rectifier is in DCM, the proposed MPC algorithm is able to regulate the line current to the reference current. As mode detection was applied, a suitable duty cycle for DCM was generated. Figure 16 shows the current waveform derived using the MPC in the 100% load condition. The MPC-regulated system is able to mirror the reference current in the CCM region without problems, due to the fast dynamic response of the control algorithm. A comparison of the waveforms generated using the two systems shows that in DCM and CCM operation, there is more distortion in the current waveforms created with the PI-controlled system than those observed with the MPC-regulated system. The mode detection applied with the MPC makes it able to control the line current optimally in each conduction mode. In addition, the dynamic response of the controller is fast enough to control AC waveforms.

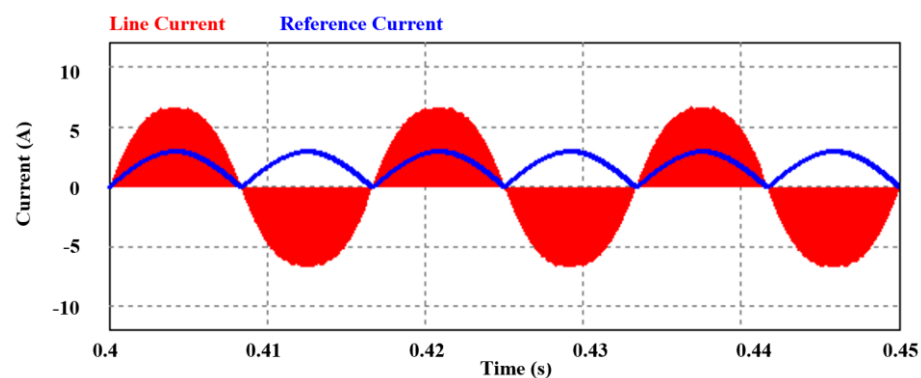


Figure 15. Current waveform derived using MPC in DCM.

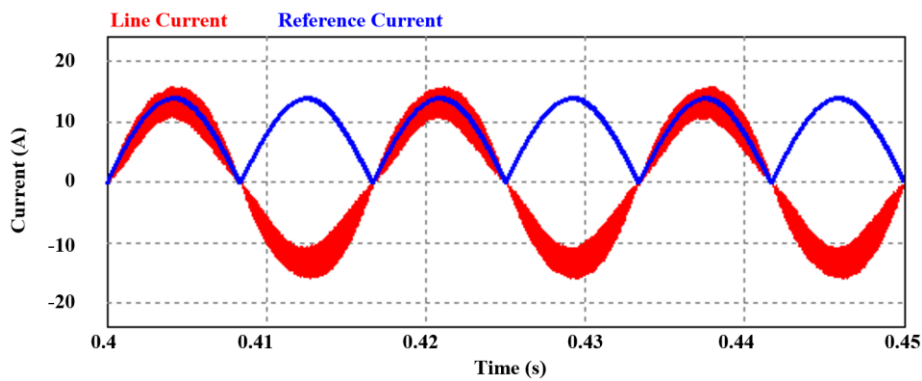


Figure 16. Current waveform derived using MPC in CCM.

Figure 17 shows the current waveform derived using PI control with a 40% load, in the time domain. In the low load region, current distortion is made worse by prolonged operation in DCM. As shown in Figure 17, it is difficult for the line current to mirror the reference current. This current distortion becomes more apparent with a low power load. In particular, the distortion is worsened near the zero-crossing point of the current. Figure 18 shows the corresponding current waveform in the frequency domain. With this figure, the harmonic components of the current can be observed.

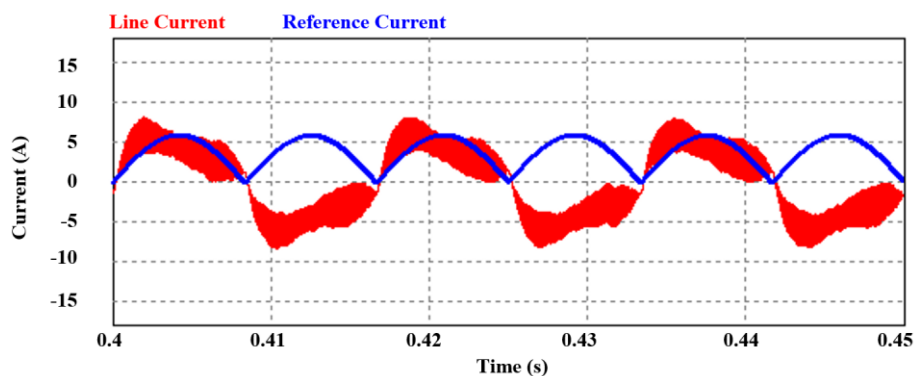


Figure 17. Time-domain current waveform derived using PI control with a 40% load.

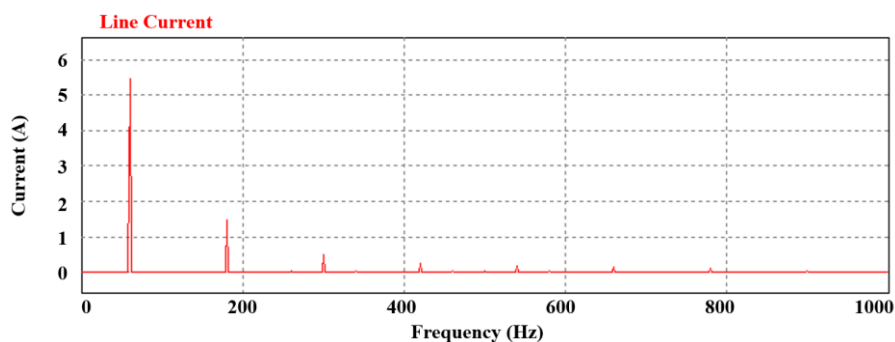


Figure 18. Frequency-domain current waveform derived using PI control with a 40% load.

Figure 19 shows the current waveform derived using the MPC with a 40% load, in the time domain. With this algorithm, the line current is closer to the reference current. The difference in current quality between the conventional and proposed algorithms can be observed at the zero-crossing points of the line current. At these points, the rate of change of current is steepest. Hence, in order to regulate this quick change, a controller with a fast dynamic response is required. The MPC deduces the optimal

duty cycle for both the CCM and DCM. Hence, unlike the PI controller, it is capable of this faster dynamic response. Figure 20 shows the current waveform derived using the MPC, in the frequency domain. In contrast to the waveform observed with conventional PI control, the magnitude of the harmonics in the MPC-regulated system is too small to observe, indicating that the MPC improves line current quality.

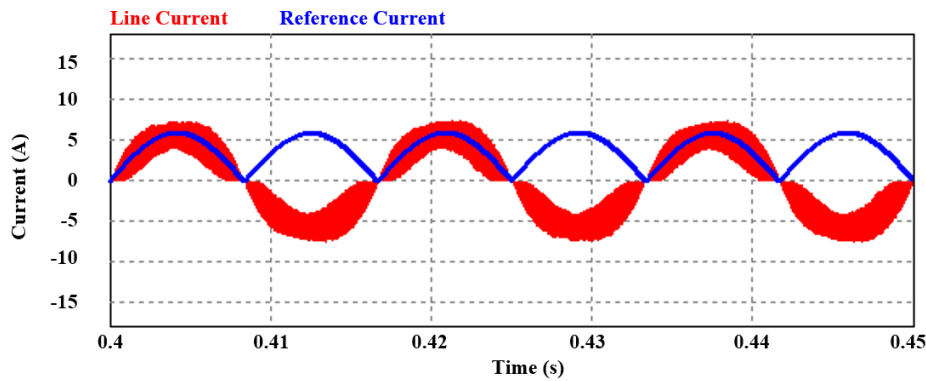


Figure 19. Time-domain current waveform derived using MPC with a 40% load.

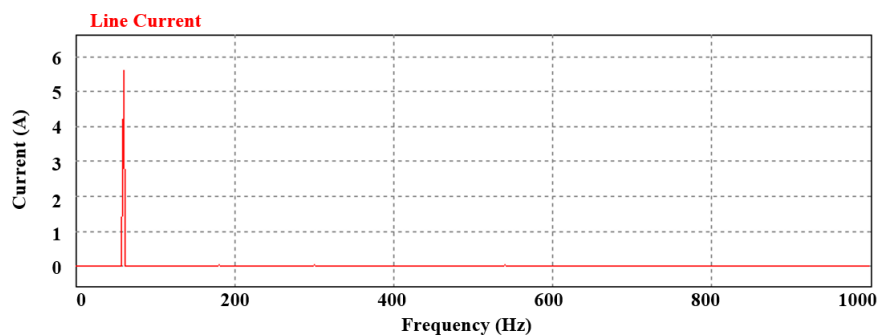


Figure 20. Frequency-domain current waveform derived using MPC with a 40% load.

Figure 21 shows the current waveform derived using PI control, with a full load, in the time domain. In high load conditions, the rectifier operates predominantly in CCM. Although, there is little DCM operation, it is possible to observe current distortion with the conventional PI control method, which is confirmed by analysis of the current in the frequency domain, as shown in Figure 22. From this image, it can be observed that the magnitude of the harmonic components generated is approximately 10% of the magnitude of the fundamental current component.

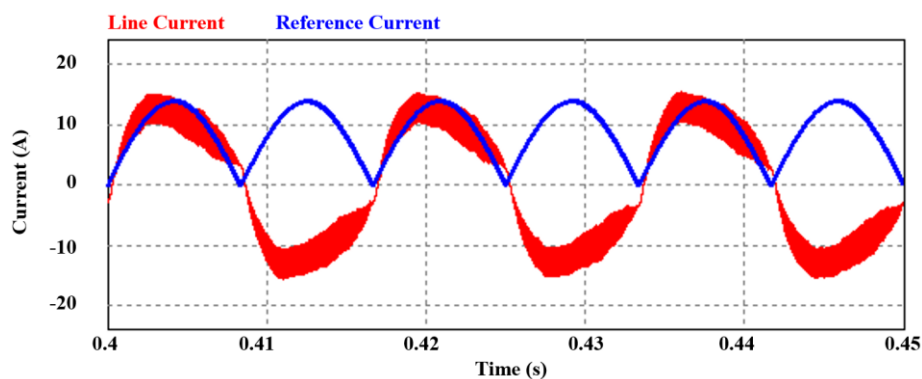


Figure 21. Time-domain current waveform derived using PI control at full load.

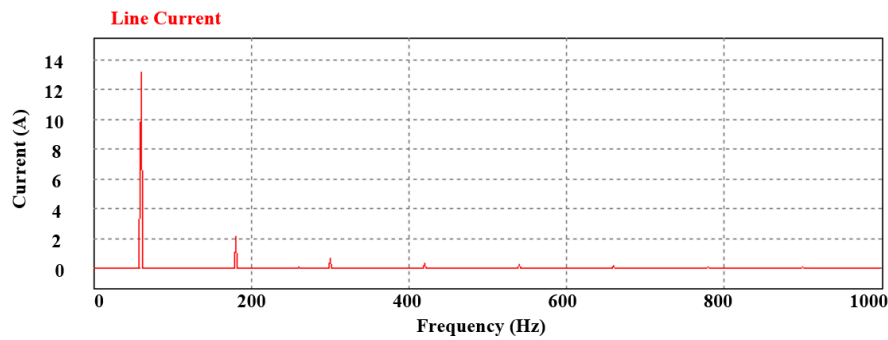


Figure 22. Frequency-domain current waveform derived using PI control at full load.

Figure 23 shows the current waveform derived using the MPC, with a full load, in the time domain. Based on this image, it can be observed that line current distortion is greatly decreased with this system, in comparison to the distortion generated with the PI-controlled system. Furthermore, the distortion near the zero-crossing point is also decreased. Figure 24 shows the corresponding waveform in the frequency domain, where only the fundamental current component can be observed. When all regions of the current waveform are considered in total, including the zero-crossing points where the line current abruptly changes, we observe that the fast dynamic response of the MPC is able to decrease line current distortion.

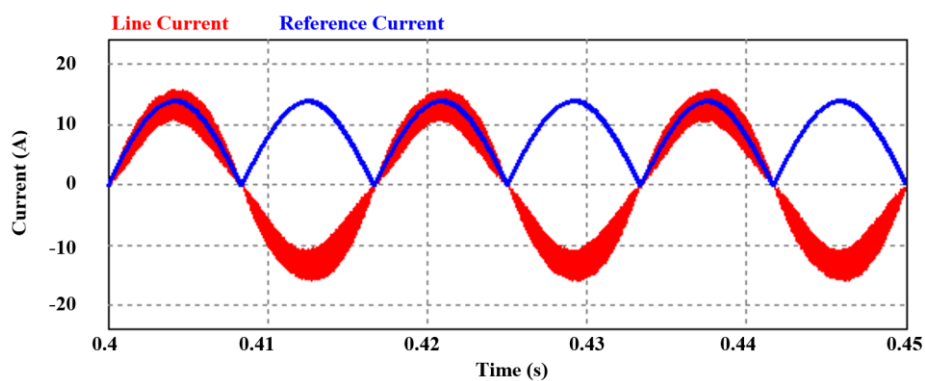


Figure 23. Time-domain current waveform derived using MPC at full load.

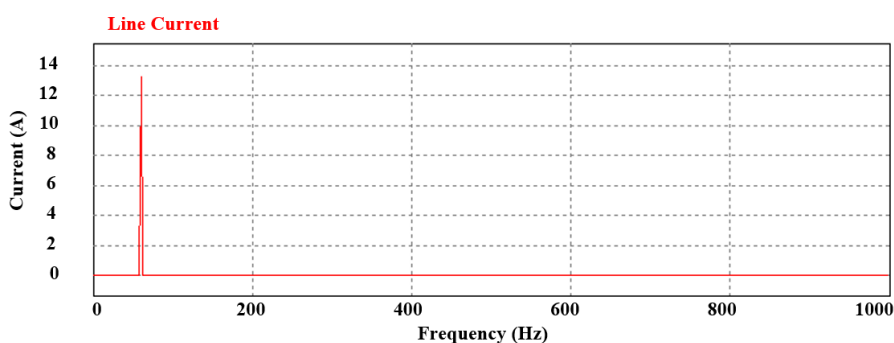


Figure 24. Frequency-domain current waveform derived using MPC at full load.

4. Experimental Section

Figure 25 shows the components used in the practical experiments. These include the single-phase Vienna rectifier prototype, depicted in Figure 25a, and the control circuitry, shown in Figure 25b, which was installed on the rectifier. The MPC algorithm was programmed on a TMS320F28335 digital

signal processor (DSP). In addition, the THD and PF were measured using a WT-3000 power analyzer (Yokogawa, Tokyo, Japan). The experimental parameters are the same as the simulation parameters.

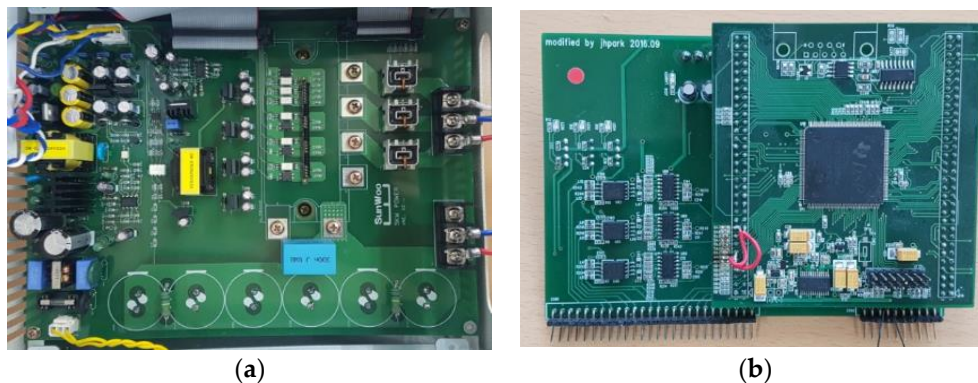


Figure 25. Components used in practical experiments. (a) Single-phase Vienna rectifier board; (b) Control board.

Figure 26 shows the line current waveform generated when conventional PI control was applied at 40% of the rated power. In this load condition, DCM operation is dominant. Hence, current distortion is appreciable due to prolonged operation in DCM. Moreover, the dynamic response of the PI controller is not fast enough to regulate the line current.

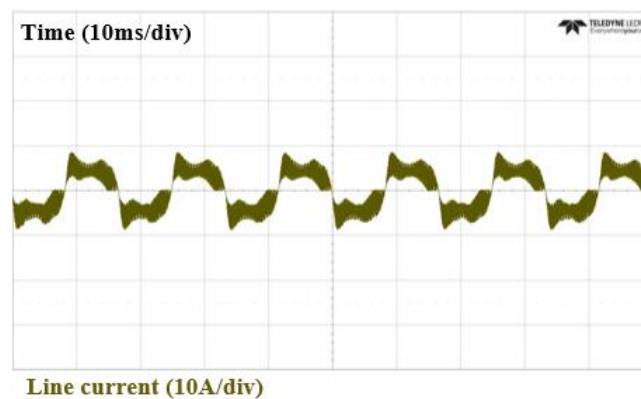


Figure 26. Line current observed using PI control at 40% of rated power.

Figure 27 shows the waveform generated when the proposed MPC algorithm was applied at 40% of the rated power. The MPC deduces the optimal duty cycle for control based on the system model, improving line current quality as a result of its fast dynamic response. This means that, with this algorithm, it is possible to improve the THD and the PF of the line current.

Figure 28 shows the current waveform observed when conventional PI control was applied at rated power. Near the zero-crossing point, where the line current changes quickly, the slow dynamic response of the PI controller induces distortion. With this method, we also observe an increase in harmonic current components and a decrease in the PF, indicating a deterioration of the line current quality. Figure 29 shows the current waveform generated when the proposed MPC algorithm was applied at rated power. In contrast to the PI-controlled system, the distortion near the zero-crossing point is decreased. This image indicates that the line current mirrors the reference current.

Figure 30 shows the transient of line current when the load is suddenly changed 60 to 100%. In this figure, it is possible to see that the transient waveform has low overshoot and fast convergence to the steady state region. Figure 31 shows the transient of line current when the load is suddenly

changed 100 to 60%. This figure shows same manner as the previous waveform. This shows that the line current is possible to control the sudden load changing without any problems.

Figure 32 shows the THD in the different load conditions. In the PI-controlled system, THD is 40.68% at 40% of the rated power, and 13.49% at the rated power. In the MPC-regulated system, THD is 16.36% at 40% of the rated power, and 5.52% at the rated power. When the load is increased, the THD is improved, regardless of if the PI controller or the MPC is applied. With the proposed MPC algorithm, the value of the THD is approximately about 7–15% lower than the value obtained with conventional PI control, in all load conditions.

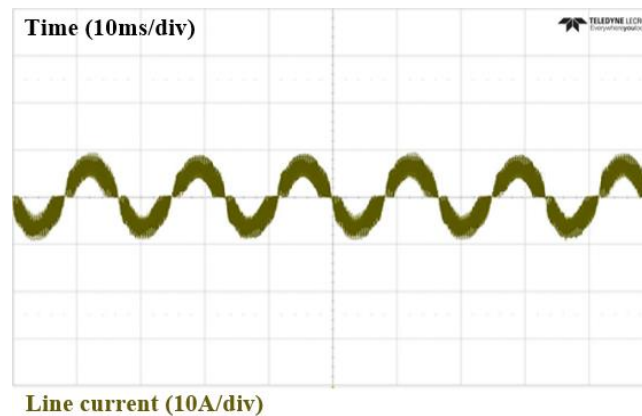


Figure 27. Line current observed using MPC at 40% of rated power.

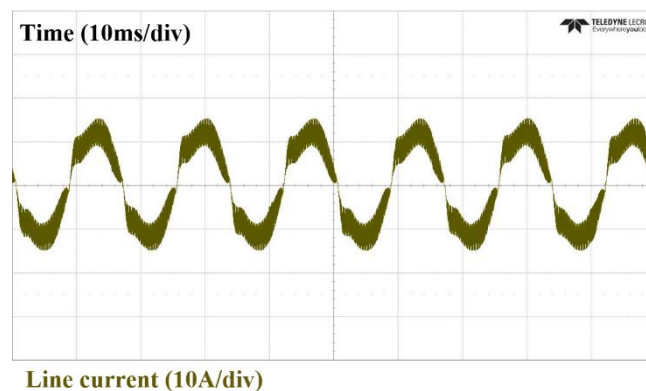


Figure 28. Line current observed using PI control at rated power.

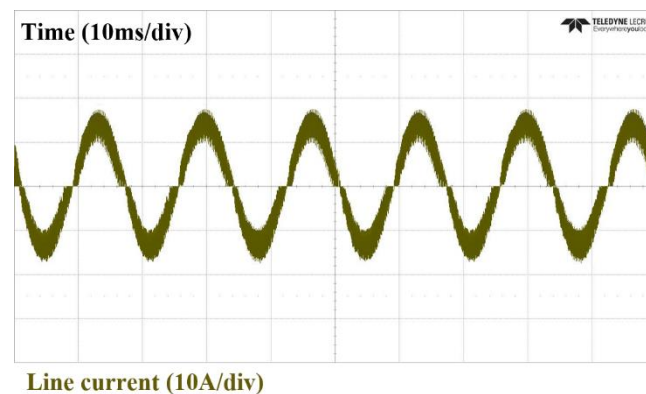


Figure 29. Line current observed using MPC at rated power.

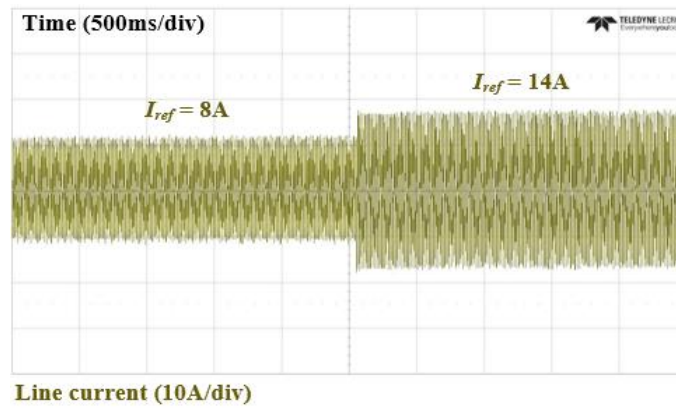


Figure 30. Line current observed load changing 60 to 100%.

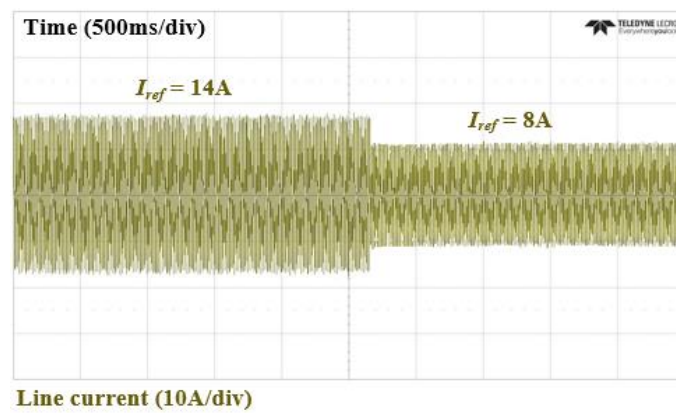


Figure 31. Line current observed load changing 100 to 60%.

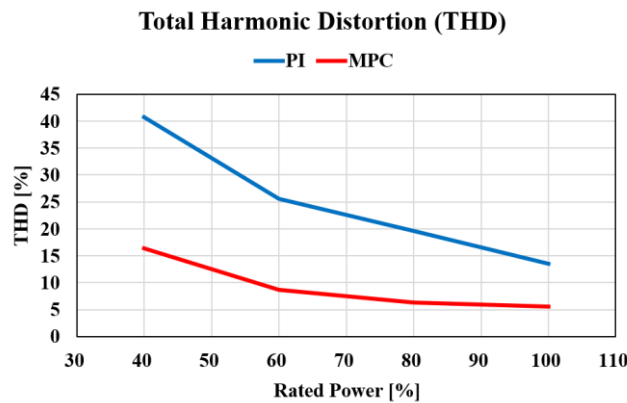


Figure 32. Total harmonic distortion in different load conditions.

Figure 33 shows the value of the PF in the different load conditions. With the PI-controlled system, the value of the PF is 0.902 with the 40% load and 0.991 at rated power. In contrast, with the MPC-regulated system, the value of the PF is 0.986 at 40% of the rated power, and 0.997 at rated power. Hence, with both control systems, the PF is brought closer to unity by increasing the load. As the fundamental current component is increased in proportion to the harmonics, the PF is improved, and THD is alleviated. The performance of the proposed MPC algorithm can thus be verified using these two figures.

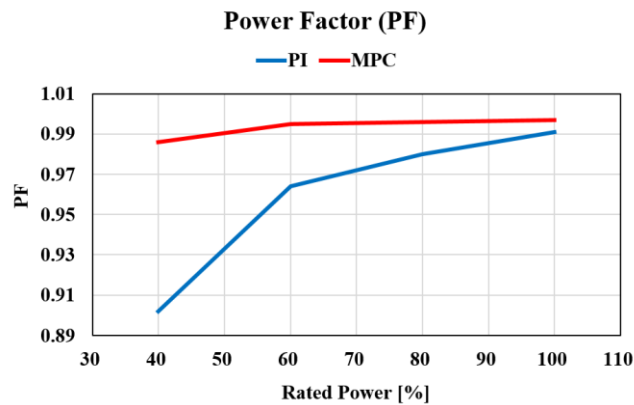


Figure 33. Power factor in different load conditions.

5. Conclusions

This paper proposes the improvement of the line current distortion for the single-phase Vienna rectifier using the model-based predictive control. Moreover, the conduction mode detection method is applied to the proposed MPC algorithm. The proposed algorithm conducts the prediction of the optimal duty cycle by using the previous and the current data of the inductor current. Therefore, this makes the proposed method possible to have the fast dynamic response, unlike the conventional PI control method. The PSIM simulation and the experimental result with the 1-kW single-phase Vienna rectifier are used for verifying the performance of the proposed algorithm. The current waveforms of the conventional method and the proposed method are compared. Moreover, THD and PF in the various load condition is measured in order to prove the validity of the proposed MPC algorithm.

Author Contributions: Kyo-Beum Lee provided guidance and supervision. Yong-Dae Kwon and Jin-Hyuk Park implemented the main research, performed the simulation and experiment, wrote the paper and revised the manuscript as well. All authors have equally contributed to the simulation analysis, experiment and result discussions.

Acknowledgments: This research was supported by a grant (No.20172020108970) from the Korea Institute of Energy Technology Evaluation and Planning (KETEP) that was funded by the Ministry of Trade, Industry and Energy (MOTIE).

Conflicts of Interest: The authors declare no conflict of interest.

Appendix

The variables, acronyms, indexes and constants defined in the manuscript is explained in the Table A1.

Table A1. Nomenclatures.

Variables/Acronyms/Indexes/Constants	Full Nomenclatures
EV	Electric Vehicle
MPC	Model-based Predictive Control
PWM	Pulse-Width Modulation
OBC	On Board Charger
THD	Total Harmonic Distortion
PF	Power Factor
FS-MPC	Finite StateModel-base Predictive Control
DSP	Digital Signal Processor
ADC	Analog to Digital Conversion
PI	Proportional-Integral
DCM	Discontinuous Current Mode
CCM	Continuous Current Mode

Table A1. Cont.

Variables/Acronyms/Indexes/Constants	Full Nomenclatures
L	Filter inductor
R	Filter Resistor
V_{Grid}	Grid Voltage
D_p	Top Diode of Vienna rectifier
D_n	Bottom Diode of Vienna rectifier
S_p	Top Switch
S_n	Bottom Switch
C_{top}	Top Capacitor
C_{bot}	Bottom Capacitor
R_{out}	Output Resistor
V_{DC}	DC Voltage
i^*	Voltage Controller Output
i_L	Sensed Inductor Current
i_L^*	Inductor Current Reference
ω_{cc}	Bandwidth of PI controller
$K_{p,current}$	Proportional Gain of PI controller
$K_{I,current}$	Integral Gain of PI controller
ζ	Damping-Ratio
i_{peak}	Peak Value of Inductor Current
i_{avg}	Average Value of Inductor Current
i_{zero}	Zero Value of Inductor Current
$S_{L,on}$	Slope during Switch on time
V_{top}	Top DC link Voltage
V_{bot}	Bottom DC link Voltage
$S_{L,bot,off}$	Slope during Bottom Switch off
$S_{L,top,off}$	Slope during Bottom Switch on
$i_{L,k+1,top}$	Next State inductor Current
$i_{L,k}$	Current State Inductor Current
$i_{err,top}$	Error of Inductor Current in CCM
$T_{on,top,CCM}$	Top Switch on Time in CCM
$Duty_{top,CCM}$	Top Switch Duty in CCM
$T_{on,bot,CCM}$	Bottom Switch on Time in CCM
$Duty_{bot,CCM}$	Bottom Switch Duty in CCM
T_{zero}	Zero drop Time of Inductor Current
$i_{L,avg,k+1}$	Average Current of Next Current
$i_{err,DCM}$	Error in DCM
$T_{on,top,DCM}$	Top Switch on Time in DCM
$Duty_{top,DCM}$	Top Switch Duty in DCM
$T_{on,bot,DCM}$	Bottom Switch on Time in DCM
$Duty_{bot,DCM}$	Bottom Switch Duty in DCM
L_0	Actual Inductance Value
L_{cal}	Nominal Inductance Value

References

1. Bak, Y.S.; Lee, E.S.; Lee, K.-B. Indirect Matrix Converter for Hybrid Vehicle Application with Three-Phase and Single Outputs. *Energies* **2015**, *8*, 3849–3866. [[CrossRef](#)]
2. Kim, J.-H.; Lee, I.-O.; Moon, G.-W. Integrated Dual Full-Bridge Converter With Current-Doubler Rectifier for EV Charger. *IEEE Trans. Power Electron.* **2016**, *31*, 942–951. [[CrossRef](#)]
3. Lee, J.-H.; Lee, J.-S.; Lee, K.-B. A Fault Diagnosis Method in Cascaded H-bridge Multilevel Inverter Using Output Current Analysis. *J. Electr. Eng. Technol.* **2017**, *12*, 2278–2288.
4. Park, J.Y.; Sin, J.O.; Bak, Y.S.; Lee, K.-B. Common-mode Voltage Reduction for Inverters Connected in Parallel Using and MPC Method with Subdivided Voltage Vectors. *J. Electr. Eng. Technol.* **2018**, *13*, 1212–1222.
5. Jeong, M.-G.; Kim, S.-M.; Lee, K.-B. Discontinuous PWM Scheme for Switching Losses Reduction in Modular Multilevel Converters. *J. Power Electron.* **2017**, *17*, 1490–1499.

6. Park, J.-H.; Yang, S.H.; Lee, K.-B. Synchronous Carrier-based Pulse Width Modulation Switching Method for a Vienna Rectifier. *J. Power Electron.* **2018**, *18*, 604–614.
7. Jeong, M.-G.; Kim, S.-M.; Lee, K.-B. An Interleaving Scheme for DC-Link Current Ripple Reduction in Parallel-Connected Generator Systems. *J. Power Electron.* **2017**, *17*, 1004–1013.
8. Yang, S.H.; Park, J.-H.; Lee, K.-B. Current Quality Improvement for a Vienna Rectifier with High-Switching Frequency. *Trans. Korean Inst. Power Electron.* **2017**, *22*, 181–184. [[CrossRef](#)]
9. Wu, H.; Zhang, Y.; Jia, Y. Three-Port Bridgeless PFC Based Quasi Single-Stage Single-Phase AC-DC Converters for Wide Voltage Range Applications. *IEEE Trans. Ind. Electron.* **2018**, *65*, 5518–5528. [[CrossRef](#)]
10. Adhikari, J.; Prasanna, I.V.; Panda, S.K. Reduction of Input Current Harmonic Distortions and Balancing of Output Voltages of the Vienna Rectifier under Supply Voltage Disturbances. *IEEE Trans. Power Electron.* **2017**, *32*, 5802–5812. [[CrossRef](#)]
11. Kim, D.-H.; Kim, M.-J.; Lee, B.-K. An Integrated Battery Charger with High Power Density and Efficiency for Electric Vehicles. *IEEE Trans. Power Electron.* **2017**, *32*, 4553–4565. [[CrossRef](#)]
12. Kwon, M.; Choi, S. An Electrolytic Capacitorless Bidirectional EV Charger for V2G and V2H Applications. *IEEE Trans. Power Electron.* **2017**, *32*, 6792–6799. [[CrossRef](#)]
13. Thangavelu, T.; Shanmugam, P.; Raj, K. Modelling and control of VIENNA rectifier a single phase approach. *IET Power Electron.* **2015**, *8*, 2471–2482. [[CrossRef](#)]
14. Lee, J.-S.; Lee, K.-B. Performance Analysis of Carrier-Based Discontinuous PWM Method for Vienna Rectifiers with Neutral-Point Voltage Balance. *IEEE Trans. Power Electron.* **2016**, *31*, 4075–4084. [[CrossRef](#)]
15. Lee, J.-S.; Lee, K.-B. Predictive Control of Vienna Rectifiers for PMSG Systems. *IEEE Trans. Ind. Electron.* **2017**, *64*, 2580–2591. [[CrossRef](#)]
16. Lee, J.-S.; Lee, K.-B. A Novel Carrier Based PWM for Vienna Rectifier with a Variable Power Factor. *IEEE Trans. Ind. Electron.* **2016**, *63*, 3–12. [[CrossRef](#)]
17. Mallik, A.; Lu, J.; Khaligh, A. A Comparative Study between PI and Type-II Compensators for H-Bridge PFC Converter. *IEEE Trans. Ind. Appl.* **2018**, *54*, 1128–1135. [[CrossRef](#)]
18. Pastor, M.-A.; Idiarte, V.-E.; Pastor, C.-A.; Salamero, M.-L. Interleaved Digital Power Factor Correction Based on the Sliding-Mode Approach. *IEEE Trans. Power Electron.* **2016**, *31*, 4641–4653. [[CrossRef](#)]
19. Kanaan, H.Y.; Al-Haddad, K.; Hayek, A.; Mougharbel, I. Design, study, modelling and control of a new single-phase high power factor rectifier based on the single-ended primary inductance converter and the Sheppard-Taylor topology. *IET Power Electron.* **2007**, *2*, 163–177. [[CrossRef](#)]
20. Malik, A.; Khaligh, A. An Integrated Control Strategy for a Fast Start-Up and Wide Range Input Frequency Operation of a Three-Phase Boost-Type PFC Converter for More Electric Aircraft. *IEEE Trans. Veh. Technol.* **2017**, *66*, 10841–10852. [[CrossRef](#)]
21. Louganski, K.P.; Lai, J.S. Current phase lead compensation in single-phase PFC boost converters with a reduced switching frequency to line frequency ratio. *IEEE Trans. Power Electron.* **2007**, *22*, 113–119. [[CrossRef](#)]
22. Kim, D.J.; Park, J.-H.; Lee, K.-B. Scheme for Improving Line Current Distortion of PFC Using a Predictive Control Algorithm. *J. Power Electron.* **2015**, *15*, 1168–1177. [[CrossRef](#)]
23. Ren, H.-P.; Guo, X. Robust Adaptive Control of a CACZVS Three-Phase PFC Converter for Power Supply of Silicon Growth Furnace. *IEEE Trans. Ind. Electron.* **2016**, *63*, 903–912. [[CrossRef](#)]
24. Youn, H.S.; Park, J.S.; Park, K.B.; Baek, J.I.; Moon, G.W. A digital predictive peak current control for power factor correction with low-input current distortion. *IEEE Trans. Power Electron.* **2016**, *31*, 900–912. [[CrossRef](#)]
25. Lee, J.-S.; Lee, S.-J.; Lee, K.-B. Torque-Ripple Reduction and Fast Torque Response Strategy for Predictive Torque Control of Induction Motors. *Int. J. Electron.* **2018**, *105*, 303–323. [[CrossRef](#)]
26. Chen, Y.L.; Chen, Y.M. Line current distortion compensation for DCM/CRM boost PFC converters. *IEEE Trans. Power Electron.* **2016**, *31*, 2026–2038. [[CrossRef](#)]
27. Ji, Q.; Ruan, X.; Xie, L.; Ye, Z. Conducted EMI spectra of average current controlled boost PFC converters operating in both CCM and DCM. *IEEE Trans. Ind. Electron.* **2015**, *62*, 2184–2194. [[CrossRef](#)]
28. Buso, S.; Caldognetto, T.; Brandao, D.I. Dead-Beat Current Controller for Voltage-Source Converters with Improved Large-Signal Response. *IEEE Trans. Ind. Electron.* **2016**, *52*, 1588–1596. [[CrossRef](#)]
29. Xia, C.; Wang, Y.; Shi, T. Implementation of Finite-State Model Predictive Commutation Torque Ripple Minimization of Permanent-Magnet Brushless DC Motor. *IEEE Trans. Ind. Electron.* **2013**, *60*, 896–905. [[CrossRef](#)]

30. Baek, J.-B.; Choi, W.-I.; Cho, B.-H. Digital adaptive frequency modulation for bidirectional DC-DC converter. *IEEE Trans. Ind. Electron.* **2013**, *60*, 5167–5176. [[CrossRef](#)]
31. Stumper, J.-F.; Hagenmeyer, V.; Kuehl, S.; Kennel, R. Deadbeat control for electrical drives: A robust and performant design based on differential flatness. *IEEE Trans. Power Electron.* **2015**, *30*, 4585–4596. [[CrossRef](#)]
32. Saxena, A.R.; Veerachary, M. Robust Digital Deadbeat Control for DC-DC Power Converter with Online Parameter Estimation. In Proceedings of the Joint International Conference on Power Electronics (PEDES), New Delhi, India, 20–23 December 2010; pp. 1–5.



© 2018 by the authors. Licensee MDPI, Basel, Switzerland. This article is an open access article distributed under the terms and conditions of the Creative Commons Attribution (CC BY) license (<http://creativecommons.org/licenses/by/4.0/>).